

1.1 Modeling, Simulation, and Experimentation of a Promising New Packaging Technology: Parallel Fluidic Self-Assembly of Microdevices

J. LIENEMANN, A. GREINER, J. G. KORVINK,
Albert Ludwig University, Freiburg Germany
X. XIONG, Y. HANEIN, K. F. BÖHRINGER, University of Washington,
Seattle, WA, USA

Abstract

The parallel fluidic self-assembly of microdevices is a new technology that promises to speed up the production of complex microsystems made up of many separate parts. The technology brings many advantages. First, it enables a mix of chipmaking technologies for each of the component parts, with each technology selected for its particular technical or financial benefits. Second, it eliminates the need for pick-and-place assembly that would unnecessarily slow down any manual assembly technique. Third, it enables massively parallel assembly, almost independent of the number of parts involved, and thereby mimics the elegant parallelism inherent in microchip circuit manufacture.

In this chapter we explore this new technology with the ultimate goal of discovering the practical limits for its practical use in manufacturing real microsystems. The driving force of the assembly process is interface surface tension, and our approach is to find the simplest models that correctly describe the attachment, orientation, and bonding of parts to a suitably prepared substrate. We follow both an analytical and a numerical approach in describing the surface tension effects, the latter mainly to gain geometrical generality, and we couple modeling and simulation with suitable laboratory experiments. The ultimate goal of this work is to find practical design rules with which to select bond site geometries and the properties of participating liquids, and to find practical tolerances for all required geometrical and rheological parameters. This chapter extensively documents all results found to date, and carefully cites other work in this area.

Keywords: self-alignment, capillary forces, micro assembly, fluidic self-assembly, surface energy, surface tension, alignment error, glue polymerization, micropart angular deflection, mirror tilting

Contents

1.1.1	Introduction	4
1.1.2	Fundamentals of Interface Tension and Wetting	6
1.1.2.1	Surface Tension and Surface Energies	6
1.1.2.2	Microscopic Picture: Intermolecular Forces	8
1.1.3	Application to Self-Alignment	10
1.1.4	Experiments	11
1.1.4.1	Preparation of Substrate and Microparts	12
1.1.4.2	Lubricant Deposition	13
1.1.4.3	Micropart Assembly	14
1.1.4.4	Alignment Errors	14
1.1.5	Modeling and Simulation	16
1.1.5.1	Analytical Models	17
1.1.5.2	Three-Dimensional Surface Simulations by Energy Minimization	23
1.1.5.3	Numerical Simulations for Geometry Design	26
1.1.5.4	Modeling of Perturbations and Non-Ideal Systems	29
1.1.6	Summary and Conclusions	38
1.1.7	Acknowledgments	39
1.1.8	References	39

1.1.1 Introduction

Recent developments, with innovative materials and processes being developed in the area of microengineering, offer the opportunity to create a large variety of functional microdevices (eg, chemical, electrical, mechanical, and optical). Promising applications, eg, in telecommunications, chemical analysis, and biomedical instrumentation require integration of such devices into single compact and robust microsystems. Monolithic integration is not applicable in building such hybrid systems, when the components' fabrication processes or the materials are incompatible. Emerging techniques in the area of micro-assembly provide a solution for microsystem integration. By taking advantage of micro-assembly techniques, we can simultaneously optimize design, fabrication processes, and materials for the microcomponents. In addition, fabrication and testing of differ-

ent microcomponents can be done independently in a parallel manner. Researchers have been investigating the adoption of conventional macroscale ‘pick and place’ methods to assemble micro- or even nanoscale components [1–4]. One major concern in these approaches is the ‘sticking effect’ between assembly manipulators and components, due to electrostatic, van der Waals, or surface tension forces [5]. Special manipulators and additional tools are required to overcome these difficulties. Another concern is that the time efficiency is limited by the number of manipulators when a large number of components is to be assembled.

Recently, techniques have been developed to achieve massively parallel assembly. Researchers have developed techniques to transfer microstructures between aligned wafers [6, 7] and later released the structures to the destined wafers. Such techniques are categorized as deterministic parallel assembly. Compared with deterministic methods, techniques applied to assemble a large number of identical microparts on specific target sites, are classified as stochastic methods. Assembly approaches in the stochastic category are also referred to as ‘self-assembly’. Different driving forces are exploited in self-assembly. By using fluidic flow and gravitation, a process was developed by Yeh and Smith to assemble trapezoidal microcomponents into matching holes in a substrate [8]. Böhringer et al. have proposed a micro-assembly approach by employing electrostatic fields as the driving force, with the aid of ultrasonic vibration to overcome and eliminate friction and adhesion [9, 10]. Surface tension, more dominant at the small scale than gravity [5], has also been employed as the driving force for assembly. Whitesides and coworkers first developed a strategy driven by capillary force to assemble simple electrical circuits [11, 12], and later three-dimensional (3D) electronic networks [13]. Srinivasan et al. extended the surface tension-driven assembly technique [11, 12] to assemble microscopic parts, ie, micromirrors, onto desired sites on silicon and quartz substrates [14, 15]. Recently, Yellen et al. [16a] reported on self-assembly exploiting ferromagnetic templates and external uniform magnetic fields as driving forces for alignment and orientation of colloidal particles onto patterned surfaces. Another example of part-to-substrate assembly was demonstrated [16] to assemble arrays of GaAs/GaAlAs light emitting diodes (LEDs) on a flexible curved substrate, and establish connections for the assembled parts.

To achieve integration of hybrid systems, an innovative self-assembly technique is developed to repeatedly applying the surface tension-driven assembly for multiple batches of parts [17, 18]. In this technique, the assembly is still driven by capillary forces, and it proceeds on specially treated hydrophobic sites on the substrate as described earlier [14, 15]. In addition, electrochemical modulation of the hydrophobicity of specific binding sites is used to alter the driving force for assembly. Therefore assembly can be controlled to take place only on desired binding sites. By repeating the process to activate different sites on the substrate for assembly, different batches of microparts can be assembled on a single substrate in a sequential manner. Electroplating is exploited as a post-assembly process to establish electrical connections for assembled components, such as LEDs.

The surface tension-driven assembly technique includes many process steps, so effects of perturbations must be investigated. One important advantage of this process is that it is possible to perform the essential steps without the use of ex-

pensive or complex equipment. Since many steps may be sensitive to dust and inhomogeneities, a discussion of the influence of defects is necessary.

Simulation is a valuable tool to determine the effect of both the setup and possible defects, which is not easily accessible by experiments at the microscale. We present calculations of the capillary driving forces occurring in the undisturbed alignment process and simulations of an alignment subjected to defects in the hydrophobic layer of the binding site and inhomogeneous hardening of the glue between micropart and binding site. The results enable the designer to determine if possible defects are negligible or if a clean room is necessary to maintain the reliability of the process. We further present a fast simulation tool for optimization of the pad geometry with respect to local minima, allowing the designer to find micropad shapes quickly with the requested assembly configuration.

1.1.2 Fundamentals of Interface Tension and Wetting

When placing a droplet of liquid in contact with a solid surface surrounded by a gaseous atmosphere three quasi two-dimensional (2D) phase boundaries form. Each of the phase boundaries consists of a transition region which we assume to be small with respect to the volumes of the phases themselves, so that an idealized description as a surface is appropriate. Similar arguments hold for the one-dimensional triple phase contact line, to be observed where three different phases touch. Note that on a length scale that approaches the dimensions of intermolecular distances in any of the three phases this picture does not hold any longer. In this chapter we do not consider the latter situation but rather assume that all phases are separated ideally.

1.1.2.1 Surface Tension and Surface Energies

In general two wetting regimes are distinguished [19].

- Complete wetting: the liquid phase (L) spreads out on the solid surface (S), to form a three-layer system consisting of solid, liquid, and surrounding medium (M).
- Partial wetting: the liquid phase remains in a finite region, to form a finite contact angle $\theta > 0$ at the contact line \mathcal{L} .

Fluidic self-assembly exploits the latter case, where the resulting forces due to minimization of the surface-free energy are the driving effect.

Any change in the surface area δA of a liquid droplet results in work W that is proportional to the surface change

$$\delta W = \gamma \delta A \quad (1)$$

where the proportionality coefficient γ is called the surface tension [20, 21]. It depends on the materials in contact at the interface.

On a curved interface separating two different materials, the pressure on either side of the interface is different: p_L is the pressure in material L and p_M the pressure in material M . We displace a surface element dA by an infinitesimal amount $\delta\zeta$ normal to the surface and pointing away from material L . Due to the volume change $\delta\zeta dA$ we have to take into account an additional work contribution, so that the total work is

$$\delta W = - \int (-p_L + p_M) \delta\zeta dA + \gamma \delta A \quad (2)$$

Note that dA denotes the infinitesimal surface element and δA is the total variation of the surface due to the displacement $\delta\zeta$. For given principal curvature radii R_1 and R_2 at a specific surface point the respective infinitesimal arclengths dl_1 and dl_2 change due to the infinitesimal displacement $\delta\zeta$ to $dl_1(1 + \delta\zeta R_1^{-1})$ and $dl_2(1 + \delta\zeta R_2^{-1})$, respectively. The surface element $dA = dl_1 dl_2$ therefore changes to

$$dA' = dl_1(1 + \delta\zeta R_1^{-1}) dl_2(1 + \delta\zeta R_2^{-1}) \approx dl_1 dl_2 (1 + \delta\zeta R_1^{-1} + \delta\zeta R_2^{-1}) \quad (3)$$

where terms of second order in $\delta\zeta$ have been discarded. The total variation in the surface therefore becomes $\delta A = \int \delta\zeta (R_1^{-1} + R_2^{-1}) dA$.

Inserting this into Equation (2) and taking into account that in equilibrium $\delta W = 0$ for arbitrary $\delta\zeta$ we get the Laplace-Young formula for surface pressure

$$p_L - p_M = \gamma (R_1^{-1} + R_2^{-1}) \quad (4)$$

In equilibrium the lhs of Equation (4) is a constant. This equation simply states that the sum of inverse principal curvature radii must be constant at any surface point. Therefore, provided that gravity effects are negligible, a small fluid droplet with free surface must assume a spherical shape in order to fulfill this requirement. When the surface is clamped along a given line (as it is the case in fluidic self-assembly by the triple phase contact line \mathcal{L}) its shape will become more complicated. In these cases one may revert to directly minimize the surface-free energy $\int \gamma dA$ under the constraint that the volume is constant, $\int dV = \text{const}$ (see [22] for more examples of constraint surfaces).

The material parameter γ is called the surface tension and can be seen as an energy per unit area. On a closed line confining any part of the surface area, γ is equal to the force per unit length on this line pointing in the direction tangential to the surface and inside the region enclosed by the line. This leads us to the specification of the contact angle at the contact line \mathcal{L} of three different bodies in contact. In self-assembly application these will be two immiscible fluids (L and M, here M stands for the second liquid phase) and a solid surface (S) as schematically drawn in Figure 1.1.1.

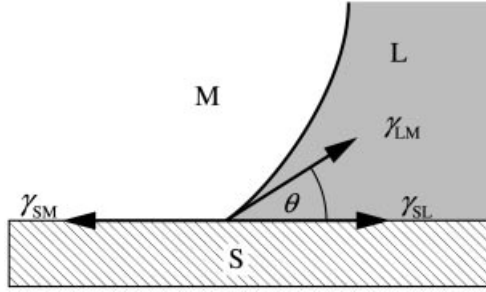


Figure 1.1.1. Contact angle due to surface tensions at the interface of three different materials.

In thermodynamic equilibrium, ie, when the contact line \mathcal{L} is not moving, the resultant force on \mathcal{L} must vanish. Thus we have

$$\gamma_{SM} = \gamma_{SL} + \gamma_{LM} \cos \theta \quad (5)$$

to determine the contact angle, which is the famous Young condition. It is used to determine the surface tensions between different materials by measuring the contact angle θ .

1.1.2.2 Microscopic Picture: Intermolecular Forces

The capillary forces present when three different phases are in contact form the main driving effect for fluidic self-assembly. Their microscopic origin derives from the intermolecular interactions.

In the case of polar molecules, dipole-dipole interactions determine the thermodynamic properties of the liquid. The dipole moment is defined as $\mathbf{u} = q\mathbf{l}$, where \mathbf{l} is the distance vector between two unit charges $+q$ and $-q$. The dipole-dipole interaction potential energy is $w(r) \propto r^{-3}$, where r is the distance between the two dipoles. It also depends on the relative orientation of the two dipole vectors with respect to each other. In a liquid these dipole molecules will rotate. Therefore, an angle averaged potential for a given distance r must be taken into account [23]. This reduces the interaction potential to the form

$$w(r) = -Cr^{-6} \quad (6)$$

where the constant C depends on the quality of the dipoles. For two molecules carrying a permanent dipole moment u we obtain $C = u^4(3kT(4\pi\epsilon_r\epsilon_0)^2)^{-1}$, with ϵ_0 denoting the permittivity of free space, ϵ_r the relative permittivity, k the Boltzmann constant, and T the absolute temperature. In case of one dipolar molecule interacting with a neutral polarizable second molecule we have $C = u^2a_0(4\pi\epsilon_r\epsilon_0)^{-2}$, where a_0 is the electronic polarizability of the second mole-

cule. And even in the case of two neutral polarizable molecules second order quantum mechanical perturbation theory leads to a contribution with $C = 3a_0^2 I (8\pi\epsilon_r\epsilon_0)^{-2}$, where I is the first ionization potential of the molecule. This latter contribution is called attraction due to dispersive forces, first described by London. It is only a rough estimate because of its restriction to spherical molecules with a unique ionization potential.

Non-polar molecules that are non-spherical have multiple ionization potentials. For large organic molecules carrying a polar bond the numerous non-polar bonds promote dispersive interactions. This in turn leads to hydrophobicity impeding the solving of specific organic molecules in water because the dispersive interaction cannot compete with the hydrogen bonds.

Due to the strong intermolecular interaction of the water molecules, special properties can be observed in water. Water molecules attract each other by *hydrogen bonds* $H \cdots O$, which are stronger than usual van der Waals forces. Hydrogen bonds derive from electrostatic interaction, but the extent of the bond is smaller than expected from van der Waals calculations. The interaction with electronegative atoms is stronger due to the small size of the hydrogen atoms and their tendency to become positively polarized and is therefore a special property of hydrogen. Furthermore, hydrogen bonds are strongly directional. The tetrahedral coordination of the water molecule (bond angle of the two covalent $H - O$ bonds is 109°) contributes to the unusual properties of water. It leads to ordering in solid water (ice) and even in the liquid, which, eventually, results in the density maximum at 4°C .

If a non-polar molecule is immersed in water, the energy of a water-water hydrogen bond is still higher than that of a van der Waals interaction. Hence, the water molecules will reorient and pack around the molecule without losing their hydrogen bond network structure, such that the least possible number of hydrogen bonds is used for adhesive interaction. This restructuring causes loss of entropy, because the water molecules are more ordered around the alien molecule, and thus makes solution of non-polar particles unfavorable.

The same effect is also responsible for immiscibility with non-polar liquids. The extraction of a single water molecule requires the breaking of four hydrogen bonds, which is highly unfavorable.

Another approach to explain surface tension is the consideration of cohesion forces. The cohesion force assigned to a single molecule depends on its potential and the number of nearest neighbors. These neighboring molecules screen the

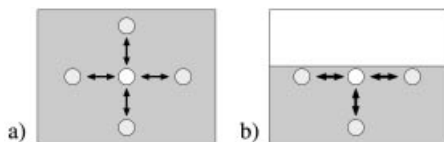


Figure 1.1.2. Cohesive forces inside (a) and on the surface (b). The molecules on the surface interact with fewer nearest neighbors and therefore are subject to a stronger lateral force. The break of symmetry causes a force, directed inwards.

electrostatic field of the molecule under investigation by reorientation of their charges. In the bulk of the droplet, the time averaged sum of the intermolecular forces is zero for symmetry reasons. No preferred direction is apparent, thus movement of molecules in all directions is equally probable, whereas on the surface the force balance in the direction normal to the surface is broken. Therefore, a force pointing inwards arises (see Figure 1.1.2). Furthermore, the number of nearest neighbors is smaller than inside the droplet, which increases the lateral stress and the desire of the surface to contract due to the loss of screening.

1.1.3 Application to Self-Alignment

At microscale, surface tension becomes more significant, and it has been exploited for various applications. High-resolution wet printing was studied by using dip-coating surfaces selectively patterned with regions of different surface tension [24, 25]. A liquid-metal micromotor was described [26], which was driven by surface tension. Building 3D hinged microstructures was accomplished by using surface tension [27]. In the self-assembly techniques described previously [11, 13–16, 18], surface tension forces are created by a liquid meniscus between hydrophobic surfaces in water to drive the assembly. A schematic illustration of the assembly process is shown in Figure 1.1.3. For the assembly, the substrate is prepared with surfaces of different surface tensions. For example [14, 15, 18], the hydrophilic substrate is prepared with hydrophobic patterns, which are Au patterns with alkanethiol self-assembled monolayer (SAM) (Figure 1.1.3 a). In order to create the driving force, the lubricant must have high interfacial energy with the surrounding medium and low interfacial energy with the SAM-coated Au surface. Due to different surface tensions, the lubricant wets exclusively the hydrophobic patterns on the substrate in water as shown in Figure 1.1.3 b. After the parts are introduced into water, as the result of minimizing the water-lubricant interfacial energy, the capillary driving force attracts and aligns the parts to

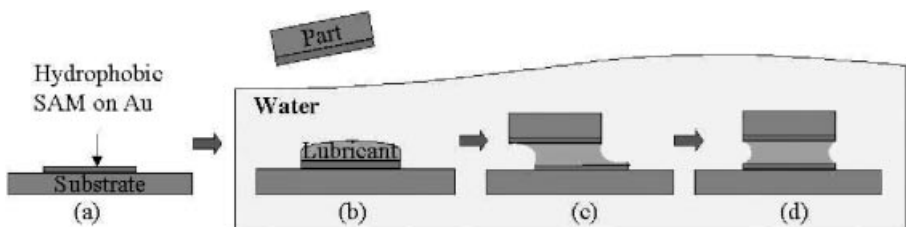


Figure 1.1.3. Self-assembly steps. (a) A fabricated substrate with the SAM-coated Au-binding site. (b) A substrate with lubricant droplets exclusively on the binding site in water. (c) After the parts are dispensed into water, the part is assembled and aligned to the binding site. (d) The lubricant can be cured to bond the part.

Table 1.1.1. Interfacial tensions γ for various material systems: M=surrounding medium; L=lubricant; S=substrate surface.

Material system (M, L, S)	γ_{ML} (mJ/m ²)	$\gamma_{SM} - \gamma_{SL}$ (mJ/m ²)
Water, TEGDMA, alkanethiol SAM	46	52
Air, water, glass [34]	72	73
Air, water, aluminum [34]	72	40
Air, Sn/Pb solder, copper [35]	504–560	213–429

the binding sites (Figure 1.1.3c). During the assembly, agitation of the parts is provided by shaking. For different applications, various lubricants have been developed including organic polymers [28] and alloy solder [16, 29, 30] in air, and the lubricant can be cured [14, 15, 18] or hardened by cooling [16] to permanently bond the parts (Figure 1.1.3d). Water surrounded by air has been used [31–33] for experimental determination of the alignment accuracy. Table 1.1.1 shows the interfacial tensions for various material systems.

In the following section, we discuss the experimental details of the self-assembly process.

1.1.4 Experiments

In this section, we describe the experimental issues of the self-assembly experiments for the purpose of investigating the self-alignment and self-assembly process. In our experiments, we demonstrate the technique by self-assembling microparts onto the specific Au-binding sites patterned on the destined substrate. To activate the binding sites, a hydrophobic alkanethiol SAM is adsorbed on the Au-binding sites. In order to perform the assembly, we first apply the lubricant onto the whole substrate, and then slide the substrate into deionized (DI) water. The lubricant forms droplets exclusively on the hydrophobic binding sites on the substrate. Next, microparts with a hydrophobic side are introduced into the water. With agitation, they are attracted and aligned to the binding sites on the substrate. Finally, the lubricant is cured to bond the parts to the substrate permanently. In the assembly process, the lubricant plays a significant role in providing the driving force, as well as in bonding the parts after assembly. Two different hydrocarbon lubricants have been used in our experiments. For assembly of multiple batches, an electrochemical surface modification technique is integrated into the process, which is discussed in detail elsewhere [18, 36].

1.1.4.1 Preparation of Substrate and Microparts

1.1.4.1.1 Test Part Fabrication

We use 1×1 mm silicon test parts for the assembly experiments. The parts are fabricated by dicing a (100) Si wafer sputtered with Cr/Au on the polished side. The gold side of the parts acts as the binding site in the assembly process (Figure 1.1.4a). The square test parts are used as fabricated without any further process. Untreated Au surfaces have a contact angle of 70° [37] after exposure to lab atmosphere, which is sufficient to ensure assembly.

1.1.4.1.2 Substrate Preparation

A silicon wafer with a thermal oxidation layer of approximately 4500 \AA is used as the substrate. Binding sites are defined on the substrate by photolithography, followed by a layer of 1100 \AA Cr/Au, sputtered on the substrate. The photoresist (AZ1512, Clariant) is then dissolved by acetone. The gold binding sites of 1×1 mm in size with 1 mm space in between are patterned on the substrate (Figure 1.1.4b). The wafer is then cleaned with isopropyl alcohol (IPA), DI water and dried with N_2 . Afterwards, we clean the substrate by oxygen plasma for 2 min. Immediately after the plasma cleaning, the substrate is immersed in 1 mM ethanolic dodecanethiol ($\text{CH}_3(\text{CH}_2)_{11}\text{SH}$, Aldrich) solution for 2–24 h, to form a hydrophobic monolayer on the gold areas. After the adsorption process, the exposed Au-binding sites turn hydrophobic with a contact angle of about 110° [37].

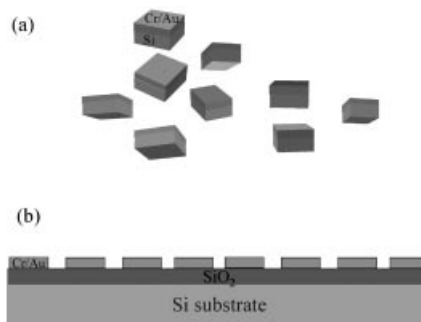


Figure 1.1.4. (a) Silicon square test parts with Au-binding site. (b) Cross section of a substrate with Au-binding sites for assembly.

1.1.4.2 Lubricant Deposition

We use two kinds of hydrocarbon polymers as lubricants for our experiments: heat curable and ultra-violet (UV) curable ones. The heat curable lubricant is composed of 97 wt.% triethyleneglycol dimethacrylate (Sigma) as the monomer, and 3 wt.% benzoyl peroxide (Sigma) as thermal initiator [38]. The UV curable lubricant is composed of 95 wt.% 1,6-hexanediol diacrylate (Aldrich) as the monomer and 5 wt.% benzoin methyl ether (Aldrich) as the photoinitiator. To prepare for assembly, we spread the lubricant over the whole substrate. The substrate is then slid vertically at a constant speed into water in a Petri dish. Due to the high water-SAM interfacial tension compared to lubricant-SAM interfacial tension, the lubricant wets exclusively the SAM-coated binding sites in water. Figure 1.1.5 illustrates the lubrication deposition step. Another method was dem-

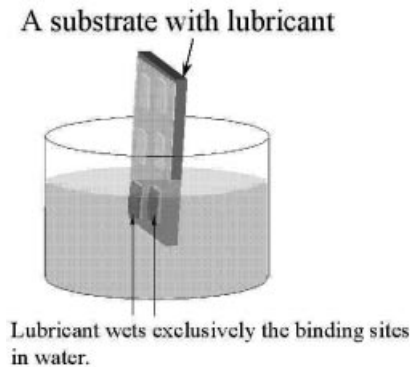


Figure 1.1.5. A substrate with the lubricant is immersed into water. The lubricant forms droplets exclusively on the binding in water.

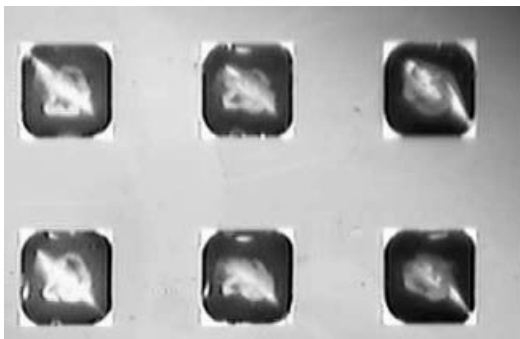


Figure 1.1.6. A substrate with an array of binding sites is immersed into water. The lubricant forms droplets exclusively on the binding sites.

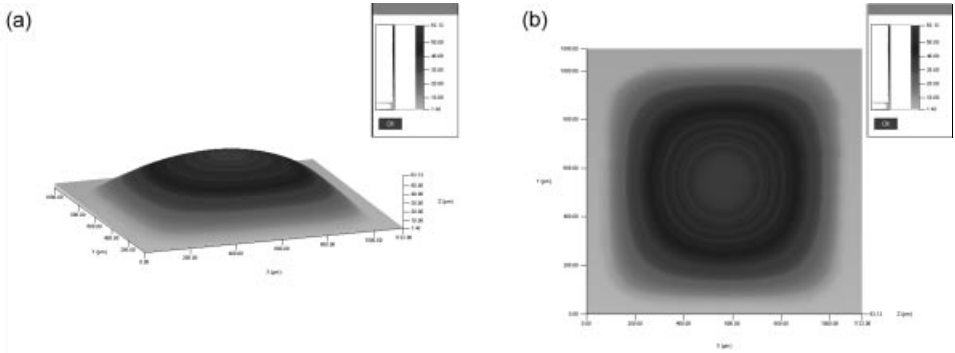


Figure 1.1.7. Surface topology of a lubricant droplet on a 1×1 mm square binding site. **(a)** The side view of surface profile of the lubricant droplet. **(b)** Top view of the surface topology; different grayscales indicate different surface heights.

onstrated by passing the substrate through a thin lubricant film on the water, therefore to coat the lubricant exclusively on the binding site [15]. For the second method, the thin lubricant film has to remain continuous during the sliding process in order for all the binding sites to have uniform lubricant coverage.

To measure the lubricant volume and thickness, we slide the substrate with the UV curable lubricant into water at a speed of approximately 3 cm/s and cure it with UV lamp for 1 h at the light intensity of $21\,000 \mu\text{W}/\text{cm}^2$. Figure 1.1.6 shows an array of square binding sites with cured lubricant. We use a surface profiler (P15, Tencor) to characterize the topology of the cured lubricant on one binding site (Figure 1.1.7). The peak point height of a cured lubricant droplet is $62.1 \mu\text{m}$, with the volume of the droplet is calculated to be 33 nL.

1.1.4.3 Micropart Assembly

After applying the lubricant, the microparts are poured into water. As soon as the part binding site has contact with a lubricant droplet on the substrate, it is aligned to the substrate binding site by the capillary driving force. The lubricant is then cured and bonds the parts to the substrate as shown in Figure 1.1.8. The polymerization process of heat curable lubricant takes approximately 1 h at 80°C in water.

1.1.4.4 Alignment Errors

An experimental study of the influence of the initial conditions and the pad shape on the alignment accuracy has been presented by Sato et al. [32, 33]. The system considered consists of water as lubricant, air as surrounding medium, and

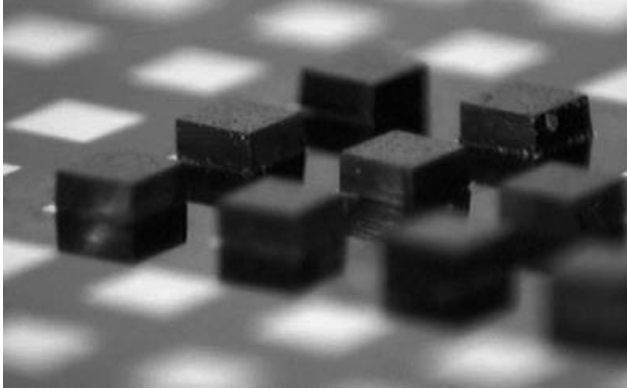


Figure 1.1.8. An array of square microparts are assembled on a substrate.

glass as binding site. The micropart is placed at a specific initial position and then released onto the lubricant droplet.

The experiments show that the final accuracy depends on many parameters. It was shown that there is an optimal value for the lubricant volume. A high volume causes a force weakening near the point of exact alignment; also, water overflow over the boundary of the highly wettable binding site occurs which further lowers the force. A lower volume enforces a good alignment due to the stronger capillary forces on the micropart. However, for a volume too low, the error was found to increase again, both for the lateral alignment and the angular rotation relative to the optimal position.

The initial lateral displacement has a lower effect on the resulting alignment, if the release position is near enough to the binding site center. For a larger displacement, the recovery of the aligned position fails, but for a system immersed in a liquid phase like for the process presented before, a better reliability can be expected. The same results are obtained for the initial distance of the micropart to the substrate. The initial angular twist displacement has only a small effect on the resulting angle.

The shape of the binding site was also found to influence the alignment error. Triangular, square, and hexagonal shapes have been examined. The hexagonal shapes showed the lowest alignment error and also were the least sensitive to an initial alignment error. The performance of the square shape was also good. The triangular shape showed a dewetting at the sharp corners of the binding site which resulted in large alignment errors.

1.1.5 Modeling and Simulation

Simulation is important for both experimentation and design. For experimentation, simulation augments our laboratory techniques by providing a way to isolate and separate physical effects, so as to test and make plausible our hypotheses on the dominant effects of interfacial interaction, by providing a way to design suitable experiments, to estimate the outcome of proposed techniques and designs, and by providing a looking-glass for data that is not otherwise easily accessible. Prudent use of simulation tools has helped us efficiently to eliminate unproductive concepts, and to explore promising new avenues.

Once verified and understood, simulation tools become essential for engineering design. In general, engineering design tools target system goals, such as manufacturability, process reliability, throughput maximization, and of course overall cost reduction. Typically, market forces dictate, so that computer-aided engineering (CAE) tools only emerge once manufacturing processes become reasonably established. Once this is the case, CAE tools can aid to rapidly spread the use of a technology, and the classical example here is circuit simulation where tools such as SPICE has brought circuit design to the smallest of enterprises making it truly ubiquitous.

Simulation for fluidic self-assembly is definitely still in the experimental phase, and the focus of work in the area is in finding the best conditions for an assembly event, and in understanding the design options available to us. As we shall see in more detail in the following sections, this includes:

- matching surface shape design,
- surface energy modeling and optimization,
- surface defect and error source modeling,
- model simplification, and
- gluing process optimization.

The current approach for surface force modeling is quasi-static. We generally assume that we are close to equilibrium, and that many dynamic effects (such as fluid flow dynamics and inertia) can be neglected. The surface shape is thus completely determined by the potential energy configuration of the system. This choice is partially dictated by the availability of simulation tools, and we mainly use:

- the *Surface Evolver* for the simulation of the geometry of fluid droplets, and
- ANSYS for the simulation of elastostatic properties of solidifying glues,

for which we have developed additional modules and coupling methods, augmented by analytical techniques. This approach has its limitations; in particular the following.

- We do not consider the assembly process in its entirety.
- We cannot consider questions involving microscopic intermolecular interactions.

Other limitations have more to do with verification, in that experimental techniques can only be expected to deliver some of the parameters that would completely verify the simulation.

The advantage of this approach is that it is computationally fast, and delivers the required results in excellent agreement with experimental observations. In addition, we avoid the costly overhead of a dedicated software implementation by using commonly available simulations tools.

1.1.5.1 Analytical Models

Analytical models provide a powerful way for optimization of a given system. Since the computational costs of evaluating of an analytical function is usually much smaller than for a numerical simulation, extensive searches in the parameter space are possible. We therefore present an analytical treatment of the necessary potential energy calculations. A comparison between analytical and numerical models is presented later in Section 5.4.

The effect of capillary forces and surface tensions can often be described by purely geometric models. The system presented consists of three interfaces: surrounding medium to solid (SM), surrounding medium to liquid (ML), and solid to liquid (SL). The potential energy is calculated by the energy integral

$$E = \int \gamma dA \quad (7)$$

over all three interfaces, where A is the interfacial area and γ the respective interfacial tension. For constant temperature and chemical composition, only spatial degrees of freedom must be considered. Gravity plays only a minor role at these length scales and can thus be neglected. In a first approach, complete wetting of the binding site is assumed. As shown in Figure 1.1.9, the meniscus between the hydrophobic binding sites provides the capillary force to self-align and self-assemble the part to the binding site on the substrate. Under different situations, different analytical models are used to calculate the interfacial areas between the meniscus and the water (see Figure 1.1.10).

As long as the distance of the micropart to the substrate is small enough compared to the lateral size, the area of the medium-liquid interface can be approximated by its projection onto the substrate plane. We first introduce a line l perpendicular to the direction of motion (see Figure 1.1.11). Then, all segments of the lubricant-medium-solid contact line \mathcal{L} on the substrate are projected onto this line. The sum w of all absolute values of these projections can then be used to

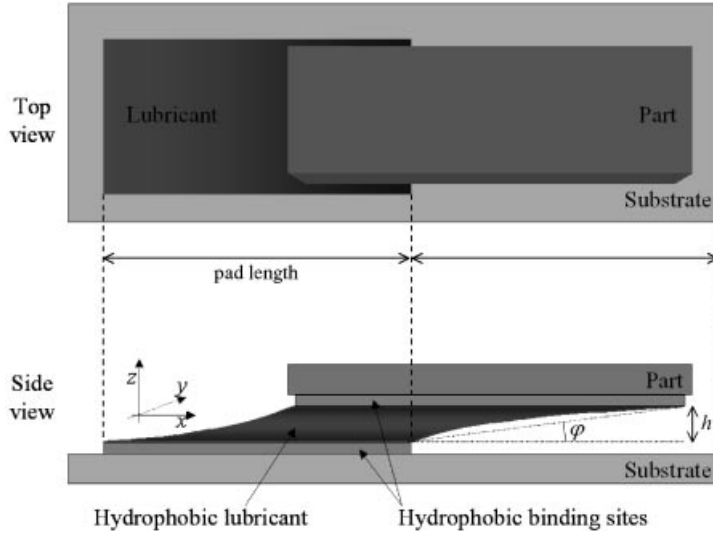


Figure 1.1.9. Top and side view of a part during fluidic self-assembly. A thin liquid film (lubricant) between the hydrophobic binding sites causes the part to align with the substrate site due to capillary forces.

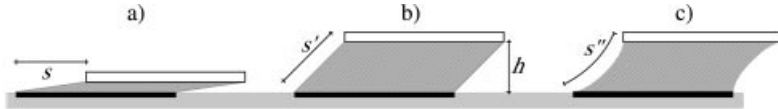


Figure 1.1.10. Approaches for calculation of surface area: (a) Projection to substrate plane, (b) plane walls, (c) curved walls: s denotes the length of the surface patch.

approximate the area change ΔA of the medium-liquid interface. Given coincident shapes of both high wettability areas of the substrate and the micropart, we obtain

$$\Delta A \approx ws \approx w|d| \tag{8}$$

where the length s of the surface patch is equal to the absolute value of the lateral displacement d (see Figure 1.1.10a). A geometric proof for a simple example is shown in Figure 1.1.11. The shaded areas show the projection of the liquid meniscus side walls to the substrate plane. The areas are shear transformed until they form a rectangle with area wd . Since shear transformations retain the area of the quadrilateral, the area of the meniscus side walls is approximately wd as well.

The surface energy is thus linear to the displacement d of the micropart, and the force $F = -dE/dd = -\gamma_{ML}w \operatorname{sgn}(d)$ is constant.

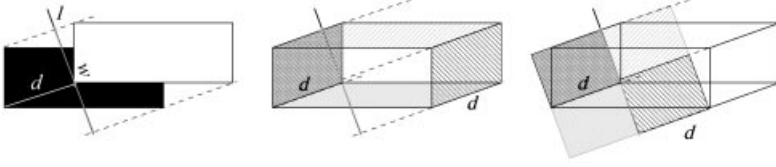


Figure 1.1.11. Geometric proof for Equation (8). The shaded areas show the projection of the liquid meniscus side walls to the substrate plane. The areas are shear transformed until they form a rectangle with area $w d$.

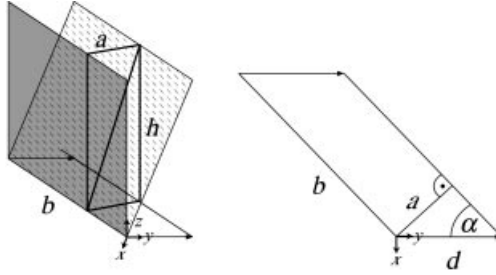


Figure 1.1.12. Calculation of area change for an area with a contact line not perpendicular to the displacement.

Near the equilibrium point of the system, ie, the point of zero micropart deflection, we cannot further assume that the lateral displacement is much larger than the height of the micropart. The projection approach is no longer valid, and a 3D treatment is therefore necessary.

For lubricant side walls where the contact line \mathcal{L} is perpendicular to the direction of displacement (ie, $a = 90^\circ$ in Figure 1.1.12), the area is

$$\Delta A = w s' = w \sqrt{d^2 + h^2} \quad (9)$$

where $s' = \sqrt{d^2 + h^2}$ is the length of the plane wall rectangle (see Figure 1.1.10b) [39]. However, if the contact line of the area is not perpendicular to the displacement, the area is sheared, thus rectangles transform to parallelograms. This makes it necessary to calculate the height of the parallelogram. In Figure 1.1.12, this corresponds to $a \neq 90^\circ$. The area of the resulting quadrilateral is $A = b \sqrt{a^2 + h^2}$ with a , b , and h as in Figure 1.1.12, resulting in

$$\begin{aligned} A &= b \sqrt{(d \sin a)^2 + h^2} = b \sin a \sqrt{d^2 + (h / \sin a)^2} \\ &= w \sqrt{d^2 + h'^2} \quad \text{with } h' = h / \sin a \end{aligned} \quad (10)$$

where a is the angle between the contact line and the displacement vector.

This yields a force of

$$F = -\gamma_{ML} wd / \sqrt{d^2 + h^2} . \quad (11)$$

For a comparison between the two models, see Figure 1.1.13. In Section 5.4 we present an extension of this model to situations with partial dewetting and apply it to the modeling of surface tension defects on the binding site.

The model can be improved further by taking into account the curvature of the surface patch. This allows for the modeling of non-planar lubricant side walls (Figure 1.1.10c).

Since the mean curvature $H = (1/R_1 + 1/R_2)/2$ with R_i as the principal radii is constant everywhere on the surface and the maximal radius R_2 is infinite at the surface points far away from the corners of the high wettability pad, we can approximate the curvature effects by a 2D model as shown in Figure 1.1.14.

With the nomenclature of Figure 1.1.14, we can determine

$$s'' = \beta R , \quad \beta = \pi - \theta_1 - \theta_2 , \quad h = h_2 - h_1 = R \cos \theta_2 - R \sin \left(\theta_1 - \frac{\pi}{2} \right)$$

and thus

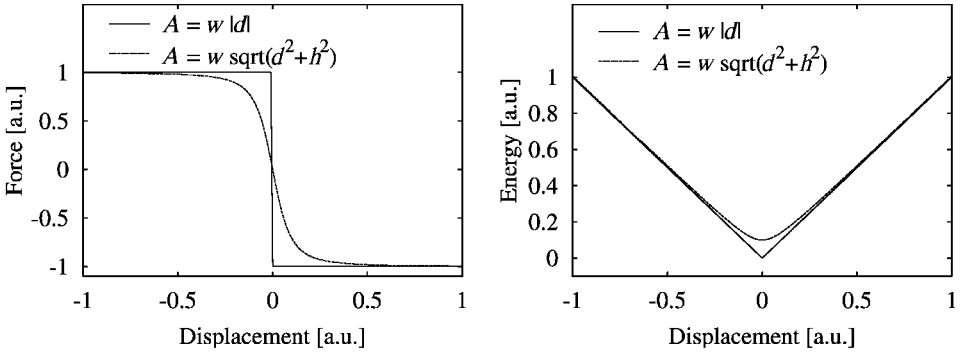


Figure 1.1.13. Driving force and surface energy results comparison by using model (8) and model (9).

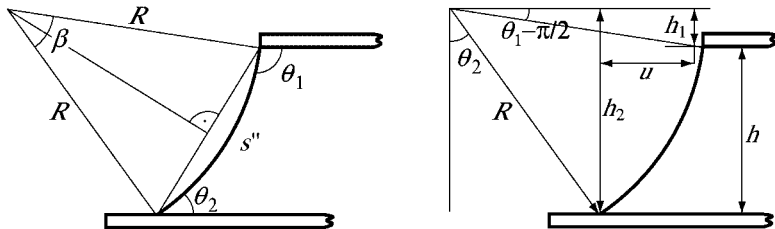


Figure 1.1.14. Schematics of a 2D model for curvature effects.

$$R = \frac{h}{\cos \theta_2 - \sin(\theta_1 - (\frac{\pi}{2}))} \quad (12)$$

This yields a surface area of

$$A = ws'' = hw \frac{\pi - \theta_1 - \theta_2}{\cos \theta_1 + \cos \theta_2}. \quad (13)$$

As in the setup presented above the contact angle θ_1 on the micropart edge is free to change, the surface will nevertheless form a plane, since this is the surface with the least area. When the micropart is deflected further from the equilibrium point, the lubricant side areas get larger, until the adhesive force of the solid-liquid interface is not strong enough to withstand the force exerted by the medium-liquid surface (see Figure 1.1.15).

As soon as the contact angle on the bottom left, $\theta_{2,l}$, drops below a certain angle θ_{dwh} , partial dewetting takes place. The contact line now follows the further displacement, and $\theta_{2,l}$ remains unchanged henceforth.

The same happens on the other side, where the contact line is pulled on the low-wetting side by the medium-liquid interface. As soon as the contact angle on the bottom right, $\theta_{2,r}$, rises above another critical angle θ_{wl} , wetting of the low wettability area occurs and $\theta_{2,r}$ keeps fixed to the contact angle on an unconstrained surface θ_w . Results of a similar model for a different micropart geometry are presented elsewhere [33].

The analytic determination of these angles in a global model is difficult, since the volume of the lubricant droplet must be held constant and thus the effect of height changes and the surface tension of the walls parallel to the displacement must be considered. However, it is possible to derive the angles in an isolated model.

For simplicity, we assume that all interfaces are either parallel to the displacement or perpendicular. With index h for the high wettability area and index l for the low wettability area, u as in Figure 1.1.14, A_h the area of the high wettability area (binding site), w_h the projection of the contact line of only the medium-lubricant interfaces pointing in the opposite direction of the displacement and $A_{ML} = A$ their area, $A_{SM,h} = (d - u)w_h$ the area of the interface medium-substrate, $A_{SL,h} = A_h - (d - u)w_h$ the area of the substrate-lubricant interface and E_0 an energy constant for all remaining surfaces, the energy of the system can be written as

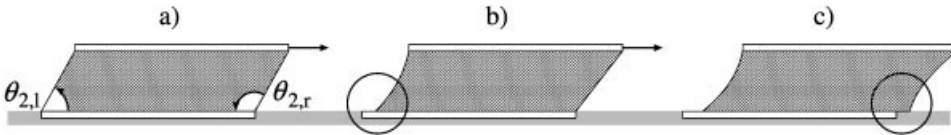


Figure 1.1.15. Partial dewetting for large displacements. (a) No dewetting, (b) dewetting of high wettability surface, (c) wetting of low wettability surface. Adapted from [33].

$$\begin{aligned}
E &= E_0 + \gamma_{\text{ML}}A_{\text{ML}} + \gamma_{\text{SL,h}}A_{\text{SL,h}} + \gamma_{\text{SM,h}}A_{\text{SM,h}} \\
&= E_0 + \gamma_{\text{ML}}hw_h \frac{\pi - \theta_1 - \theta_2}{\cos \theta_1 + \cos \theta_2} + \gamma_{\text{SL,h}}(A_h - (d - u)w_h) + \gamma_{\text{SM,h}}(d - u)w_h
\end{aligned} \tag{14}$$

using $u = R(\sin \theta_1 - \sin \theta_2) = h \frac{\sin \theta_1 - \sin \theta_2}{\cos \theta_1 + \cos \theta_2}$ and summing up all terms independent of θ_1 and θ_2 to E'_0 ,

$$E = E'_0 + hw_h \frac{\gamma_{\text{ML}}(\pi - \theta_1 - \theta_2) + (\gamma_{\text{SL,h}} - \gamma_{\text{SM,h}})(\sin \theta_1 - \sin \theta_2)}{\cos \theta_1 + \cos \theta_2} \tag{15}$$

The energy has a minimum for

$$\theta_2 = \theta_{\text{dwh}} = \pi - \arccot \frac{\gamma_{\text{SM,h}} - \gamma_{\text{SL,h}}}{\sqrt{\gamma_{\text{ML}}^2 - (\gamma_{\text{SM,h}} - \gamma_{\text{SL,h}})^2}} \quad \text{and} \quad \theta_1 = \pi - \theta_2 \tag{16}$$

With the same method, we can determine for the right side

$$\theta_{\text{wl}} = \pi - \arccot \frac{\gamma_{\text{SL,l}} - \gamma_{\text{SM,l}}}{\sqrt{\gamma_{\text{ML}}^2 - (\gamma_{\text{SL,l}} - \gamma_{\text{SM,l}})^2}} \tag{17}$$

Since for both calculations $\theta_1 = \pi - \theta_2$, the surfaces are again plane.

Once both dewetting of the high wettability area and wetting of the low wettability areas have taken place, all angles as well as u do not change any more. Thus, the force is only determined by the energy change due to the wetting of the low-wettability area $(\gamma_{\text{SL,l}} - \gamma_{\text{SM,l}})w_l(d - u)$ and the energy change due to the wetting of the high-wettability area $(\gamma_{\text{SM,h}} - \gamma_{\text{SL,h}})w_h(d - u)$. Using Equation (14) and adding the energy change due to the wetting of the low wettability area, we find a constant force

$$F = -dE/dd = -(\gamma_{\text{SL,l}} - \gamma_{\text{SM,l}})w_l - (\gamma_{\text{SM,h}} - \gamma_{\text{SL,h}})w_h \tag{18}$$

with w_l the projection of the contact line of only the medium-lubricant interfaces pointing in the direction of the displacement.

A model for the complete process thus includes a distinction depending on the contact angles on the substrate. For a small displacement, Equation (11) may be applied. For large displacements, dewetting of the high wettability area and wetting of the low wettability area takes place, and Equation (18) must be applied. However, for the Water/TEGDMA/SAM material system presented above, no continuous dewetting takes place, since the argument of the arccot function in Equation (16) is complex. Thus Equation (11) can be applied over a wide range of displacements, until a sudden snap-through of the contact line to a dewetted position takes place.

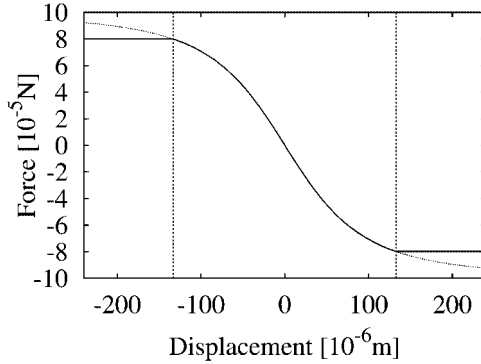


Figure 1.1.16. Force curves for Equations (11) and (18). The parameters are $w_l = w_h = 1$ mm, $h = 100$ μm , $\gamma_{\text{SM},h} = \gamma_{\text{SL},l} = 40$ mJ/m^2 , $\gamma_{\text{SL},h} = \gamma_{\text{SM},l} = 0$ and $\gamma_{\text{ML}} = 50$ mJ/m^2 . The critical angles are $\theta_{\text{dwh}} = 0.643 = 36.9^\circ$ and $\theta_{\text{wl}} = 2.498 = 143^\circ$, which yields an equivalent displacement of 133 μm (marked in the graph as vertical line).

Figure 1.1.16 shows an example for the resulting force curve for another system with γ_{ML} larger than $\gamma_{\text{SL},l} - \gamma_{\text{SM},l}$. At a displacement of 133 μm , dewetting starts. Near the alignment point, a force weakening is visible, which may slow down the alignment process. Local minima caused by defects may even impede correct alignment. This force weakening also happens for systems without continuous dewetting.

1.1.5.2 Three-dimensional Surface Simulations by Energy Minimization

Systems with complex shapes or with different high wettability areas on the substrate and micropart often give unsatisfactory results with the models presented above. Numerical simulations allow for the modeling of the complete surface and thus include curvature and nonlinear effects.

One of the most useful programs for the study of surface shapes is the *Surface Evolver* by K.A. Brakke. It ‘evolves’ the surface, which is discretized by a union of triangles, to an energy minimum by gradient descent minimization. Different minimization schemes like steepest descent and conjugate gradients are available just as are second order schemes using the Hessian matrix.

The energy may not only consist of surface tension, but also gravity, a crystalline integrand, squared mean curvature, user-defined surface integrals, and many other energy quantities can be used. It is freely available and provided with extensive documentation [40, 41].

The energy minimization is done with an explicit minimization scheme. An artificial time dependency is introduced by using the energy gradient of the surface triangle vertices as a velocity. For a triangle with edges \vec{s}_0 and \vec{s}_1 , the facet energy due to surface tension γ is calculated by

$$E = \frac{\gamma}{2} \|\vec{s}_0 \times \vec{s}_1\| \quad (19)$$

The gradient for the first edge \vec{s}_0 is then

$$\vec{g}_{s_0} = \frac{\gamma}{2} \frac{\vec{s}_1 \times (\vec{s}_0 \times \vec{s}_1)}{\|\vec{s}_0 \times \vec{s}_1\|} \quad (20)$$

Summing up all gradient parts of the adjacent faces yields the total free energy gradient of the vector motion.

Iterating this process finally yields a minimal energy surface. We apply this technique to the liquid lubricant meniscus below the micropart by constraining the liquid edges to match the setup geometry. Moving the micropart constraints slightly and evolving the surface to a minimal energy state finally yields a graph of potential energy versus micropart position. We hereby assume that the meniscus shape always goes through an energy minimum, ie, the fluid shape follows adiabatically.

The derivative of the potential energy curve to the micropart position gives insight on the forces acting on the micropart during the motion.

1.1.5.2.1 Simulation of Capillary Forces

The strengths of the capillary forces during the alignment process are crucial for getting a well-aligned position of the micropart. Figure 1.1.17 shows the displacements of all degrees of freedom of the micropart. They consist of a shift of the micropart against the binding site (x and y direction), a lift of the micropart in the direction perpendicular to the binding site, a twist rotation about the z axis and a tilt about the x and y axis. For all degrees of freedom, the system must provide a unique and distinct well-defined energy minimum with high gradient.

In our simulations we calculated the total surface energy for different displacements and lubricant volumes [42]. Figure 1.1.18a shows the potential energy and the force with respect to a lift displacement perpendicular to the binding size surface for a lubricant volume of 200 nL. The energy minimum and therefore the

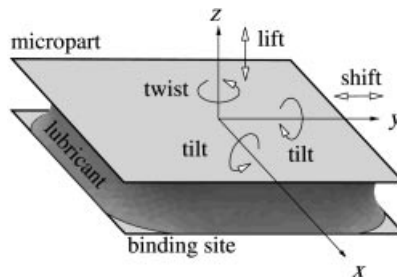


Figure 1.1.17. Geometric setup and part displacements with respect to binding site.

equilibrium position is found at a distance of 0.174 mm between the binding site and the bottom of the micropart. A large restoring force results in a system rather stiff against lift displacement.

Figure 1.1.18b shows the potential energy and restoring torque for a tilt displacement. Since the torque increases rapidly already for small tilt angles, a good parallel alignment is ensured. Lift and tilt displacements are rather uncritical, as long as the lubricant volume is not exceedingly high.

The results for a shift misalignment are shown in Figure 1.1.19a. Three different lubricant volumes were investigated. As predicted by the analytic model, the restoring force shows an increase linear with the shift displacement and then sat-

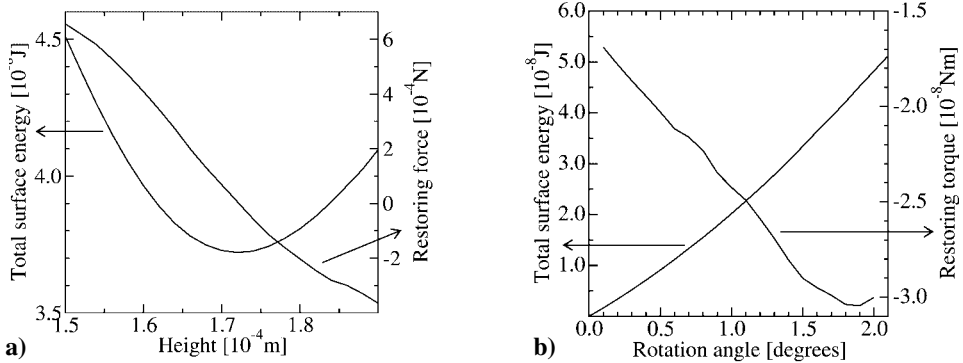


Figure 1.1.18. Capillary forces for lift and tilt displacements. The lubricant volume is 200 nL. (a) Lift along the z axis, potential energy (left scale) and capillary force (right scale). (b) Tilt of the micropart about the y axis, potential energy (left scale) and torque (right scale).

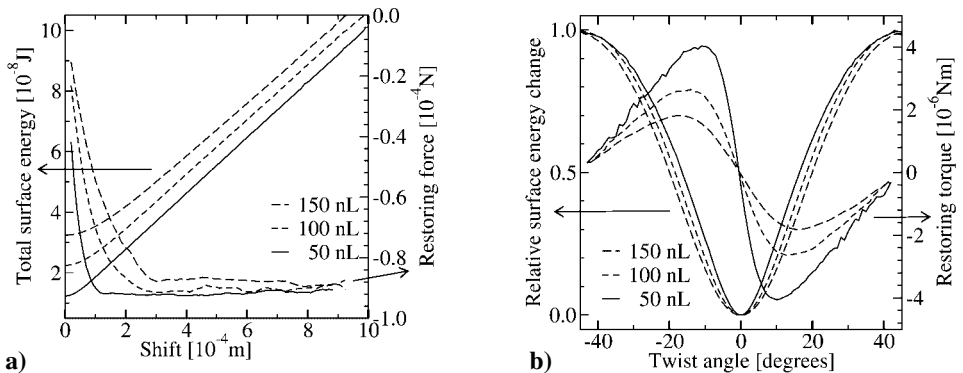


Figure 1.1.19. Capillary forces for shift and twist displacements. (a) Shift along the y axis, potential energy (left scale) and capillary force (right scale). (b) Twist about the z axis, relative potential energy $e(\phi_z) = (E(\phi_z) - E(0^\circ)) / (E(45^\circ) - E(0^\circ))$ (left scale) and torque (right scale).

urates at a constant level for higher deflection. Both the final saturation level and the force increase and thus the final alignment precision are smaller for higher volumes in accordance to experiments and the analytic model. A detailed comparison between the analytic model and numerical results is presented in Section 5.4 below.

The same results are obtained for twist displacement (Figure 1.1.19b); an increasing lubricant volume causes a force and torque weakening, which is also confirmed by experiments [42]. This force weakening may lead to a greater sensitivity to slight imperfections which form local energy minima at misaligned states. The impact of those imperfections is discussed in Section 5.4.

1.1.5.3 Numerical Simulations for Geometry Design

Since the driving force is created between hydrophobic surfaces, the design of the hydrophobic assembly patterns is of great significance in achieving a unique energy minimum and thus good assembly result. For simplification, a fast simulation tool is used to evaluate different designs. As shown before in Figure 1.1.9, the first order approximation of this area is the projection of the interfacial surface onto the substrate plane, as long as the separation between the binding sites is small compared to their lateral size. We can obtain the model of the interfacial energy in terms of overlap area as follows:

Let S and P be the substrate and part binding sites, respectively. The lubricant meniscus occupies a volume that, when projected onto the substrate plane, is given by $S \cup P$ (this assumes that S and P are not completely non-adjacent). Then, the projected surface M of the lubricant meniscus is $(S - S \cap P)$ and $(P - S \cap P)$, and its area can be calculated as

$$M = |S - S \cap P| + |P - S \cap P| = |S| + |P| - 2|S \cap P| \quad (21)$$

The surface energy which is proportional to the surface area is given by

$$W = \gamma(|S| + |P| - 2|S \cap P|) \quad (22)$$

Here γ is the proportionality factor (interfacial energy coefficient). Since the terms $|S|$ and $|P|$ in Equation (22) are constants, W is determined by $|S \cap P|$: the overlap area between S and P . When S and P coincide perfectly, W is zero. These values are in good accordance with estimates derived from the 3D surface energy minimization analysis discussed above.

This model has the further advantage that it accurately describes the situation after the initial contact of the micropart with the lubricant. For non-convex binding site shapes, multiple menisci may be involved, with severe consequences for the uniqueness of the energy minimum uniqueness. It enables the designer to estimate the energy of a system where the meniscus is confined at the overlap of the two hydrophobic areas.

To describe briefly the implementation of the simulation tool, the overlap area called $A(x, y, \theta)$ is computed with respect to three parameters, representing the relative location (x, y) and orientation θ of P to S . For a given orientation θ , the value A can be calculated efficiently by 2D convolution of P to S . To characterize the overlap area as a function of the rotation angle, calculations are iterated for discretized θ values in the range 0° to 360° . Therefore, for a binding site design, we use two plots to show the simulation results: translation and rotation. In the translation result, the overlap ratio, which is the ratio of the overlap area to part binding site area $\left(\frac{|S \cap P|}{|P|}\right)$, is plotted as a function of relative location (x, y) of P to S . In the rotation result, each point in the plot corresponds to a maximum overlap ratio with respect to a given orientation θ . An example of the simulation of a square pattern is shown in Figure 1.1.20. A comparison between simulation and experimental results of different binding site designs is investigated elsewhere [43].

In case when the parts have pre-determined design, we have to decide what is the optimal design for the binding site on the substrate. For example, the binding site design for assembly of the off-shelf LEDs with the hydrophobic pattern shown in Figure 1.1.21 a is not straightforward. If we choose the substrate bind-

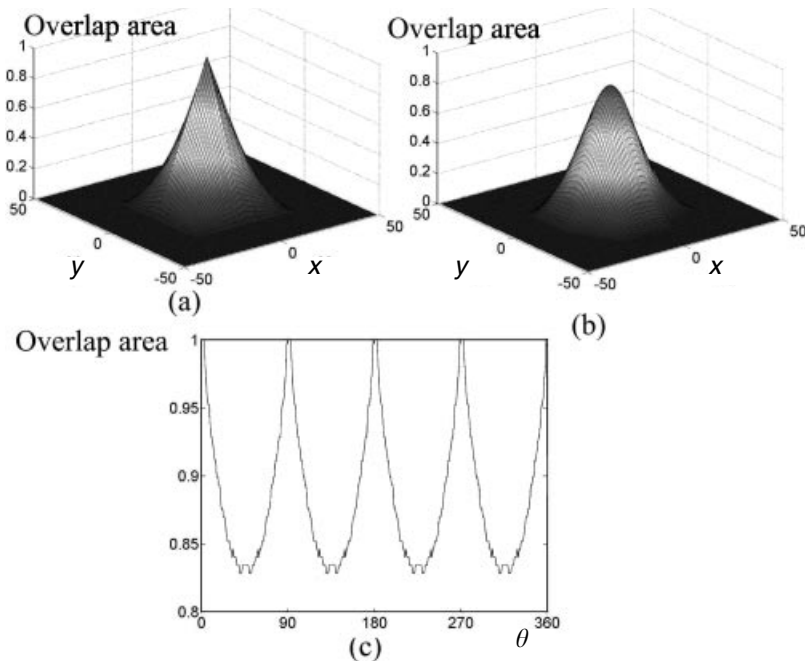


Figure 1.1.20. Simulation results for the square pattern. (a) Translation simulation of two squares with relative orientation of 0° . (b) Translation simulation of two squares with relative orientation of 45° . (c) Rotation simulation of two squares.

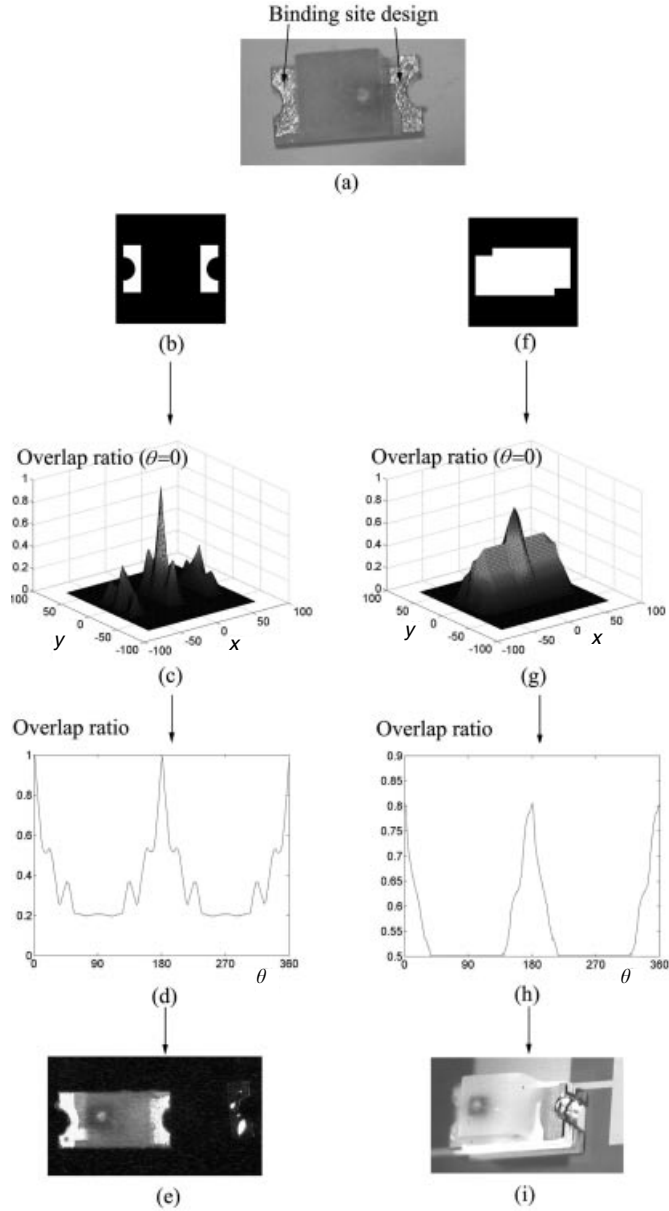


Figure 1.1.21. (a) A commercial LED with the given binding site design. (b) An intuitive design for the substrate binding site is the same as the binding site pattern of the LED. (c) Translation and (d) rotation simulations for the design in (b). (e) An LED assembled on a binding site as shown in (b) with misalignment, which corresponds to the local maximum in the translation simulation result in (c). (f) Another binding pattern design for LED assembly, with the openings on the top-left and bottom-right corners for placing the electroplating bases. (g) Translation and (h) rotation simulations for the design shown in (f). (i) An assembled LED on a binding site as shown in (e).

ing site the same as the LED's (Figure 1.1.21 b), the simulation results in Figure 1.1.21 c, d show the local overlap maxima, which corresponds to energy minima. The experimental result in Figure 1.1.21 d shows the part stuck at the position as indicated in the simulation (Figure 1.1.21 c). An improved design is shown in Figure 1.1.21 f, which has openings in the top-left and right-bottom corners for post-assembly process [17, 18]. It has no isolated minima in the translation result (Figure 1.1.21 g). The minima in the rotation result at 180° , shown in Figure 1.1.21 h, can not be avoided due to the given LED symmetry design. Figure 1.1.21 i is an assembled LED on the improved binding site.

In summary, the simulation results agree with the experiment results. The simulation tool can be employed to efficiently evaluate designs for assembly experiments in order to improve the assembly results.

1.1.5.4 Modeling of Perturbations and Non-Ideal Systems

The process of preparing the substrate and the microparts involves many process steps, including lithographic patterning and monolayer deposition. In usual fabrication environment, these processes are sensitive to perturbations like non-uniform SAM coverage, dust on the substrate or the lithography mask, blebs, light interferences, particles in the lubricant, irregular hardening of the lubricant, surface stress [44], or phase transitions [45]. We have modelled two possible errors due to these disturbances.

- Modulations of the interfacial tension of the interface between lubricant and substrate.
- Inhomogeneous hardening of the lubricant.

The former may lead to a shift of the local minimum, resulting in a misaligned equilibrium position. The latter may cause a tilt of the micropart during the hardening process.

For both simulations, we assumed that the alignment or hardening process happen on a much larger timescale than the fluidic relaxation of the lubricant droplet, ie, the fluid shape follows adiabatically.

1.1.5.4.1 Surface Tension Defects

The effect of SAM disturbances is modeled by introducing a position-dependent interfacial tension $\gamma_{\text{SL}}(\vec{r}) = \gamma_0 + \gamma_{\text{D}}(\vec{r})$, where the defect amplitude $\gamma_{\text{D}} = \gamma_{\text{D,SL}} - \gamma_{\text{D,SM}}$ with $\gamma_{\text{D,SL}}$ the defect amplitude for the interface lubricant-substrate and $\gamma_{\text{D,SM}}$ the defect amplitude for the interface surrounding medium-substrate. Due to the symmetry of the setup and the neglect of gravity, defects on the substrate and micropart can be considered equivalent. Two typical defect geometries have been investigated [46].

- Pointlike defects. A good approximation is given by

$$D(x, y) = \frac{1}{a_x(x - x_0)^2 + a_y(y - y_0)^2 + 1} \quad (23)$$

This shape function has a rotational symmetry for $a_x = a_y$, a maximum height of 1 at (x_0, y_0) and a width (at a level of 0) of $2/\sqrt{a_x}$ in x direction and $2/\sqrt{a_y}$ in the y direction.

- Line defects, modeled by the shape function

$$D(x, y) = \frac{1}{a_x(x - x_0)^2 + 1} \quad (24)$$

The pointlike defect can be used to model defective spots on the high wettability layer, where dust or blebs lead to the absence of the SAM on a small spot. Line defects can arise from light interferences or surface stress, when the gold layer or the self-assembly of the monolayer are disturbed on a larger scale.

These defects lead to a partial dewetting of the highly wettable area on the binding site. For a line defect example, the analytic model was modified to account for this dewetting by modifying the calculation of the wetted area on the substrate, using trapezoidal surfaces perpendicular to the line defect and accounting for height changes of the micropart.

We use Equation (7) to draw the balance of the interfacial energies. Using the nomenclature of Figure 1.1.22 and x_d for the defect center position, we get the following energy contributions

Trapezoidal faces (1)	$E = \gamma_{ML} h \frac{a + b}{2}$ each
Covered solid (2,3)	$E = \gamma_{SL} c(a + b)$
Uncovered solid (4,5)	$E = \gamma_{SM} c(b - a)$
Defect (4)	$E = \gamma_D c l_d$

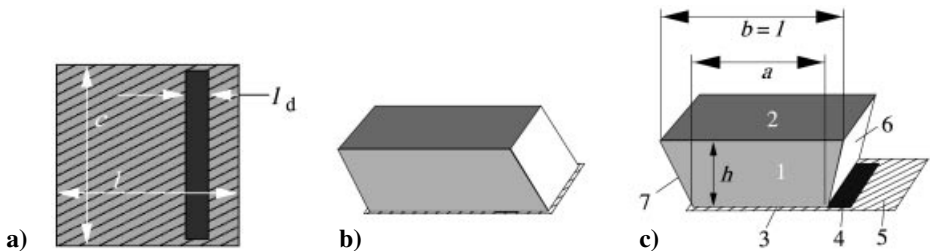


Figure 1.1.22. Analytic model for partial dewetting. (a) Line defect on the substrate high wettability area. (b) Complete wetting, (b) partial dewetting of the binding site.

$$\begin{aligned} \text{Front side (6)} \quad E &= \gamma_{\text{ML}} c \sqrt{\Delta d^2 + h^2} \\ \text{Back side (7)} \quad E &= \gamma_{\text{ML}} c \sqrt{(\Delta d + b - a)^2 + h^2} \end{aligned}$$

plus an additional energy offset to adapt the model to numerical results. The length a can be calculated from the defect geometry with

$$a = x_d - l_d/2 + l/2 \quad (25)$$

The height of the micropart must be calculated such as to fulfill the volume constraint, ie,

$$\frac{a+b}{2} ch = V \quad (26)$$

This leads to a ratio of the height h_c for a covered defect and h_u for an uncovered defect of

$$\frac{h_u}{h_c} = \frac{2l}{a+l} \quad (27)$$

For the numerical simulation, it is important to discuss the time response of the system. Since the system is much stiffer for tilt, twist and lift than for shift [42], it is possible to separate the timescales of the lateral motion (ie, in x and y direction) from the timescale of the remaining degrees of freedom. This has the effect that the lateral movement always goes through an energy minimum for the other tilt, twist and lift.

The simulation loop thus starts with finding the equilibrium for the rotation angles and the z position by using a Newton minimization scheme, and then moving the micropart by a small amount in the lateral direction.

Figure 1.1.23a shows the effect of a 0.1 mm line defect in the center of the binding site for different defect amplitudes. The micropart was first placed at an x position of -0.3 mm, then advanced to 0.3 mm in steps of 0.01 mm and returned back to -0.3 mm. The y position was always set to zero.

Even for very high defect amplitudes, no alteration of the curve is visible except for an overall energy increase contributed by the defect.

This behavior changes when the defect is placed at the binding site edge. In Figure 1.1.23, the energy minimum is shifted to the left side of the graph, since the defect impedes wetting of the edge and thus the effective pad extent is smaller. Due to the smooth defect shape, the minimum moves left with increasing defect energy.

If the defect moves further to the center again, wetting of the binding site becomes position and defect amplitude dependent. In Figure 1.1.24, the defect is placed at an x position of 0.4 mm. For small defect amplitudes, the energy curve is like that in Figure 1.1.23a. For very high defect amplitudes, the minimum is shifted to the left as in Figure 1.1.23b. Intermediate defect levels cause the en-

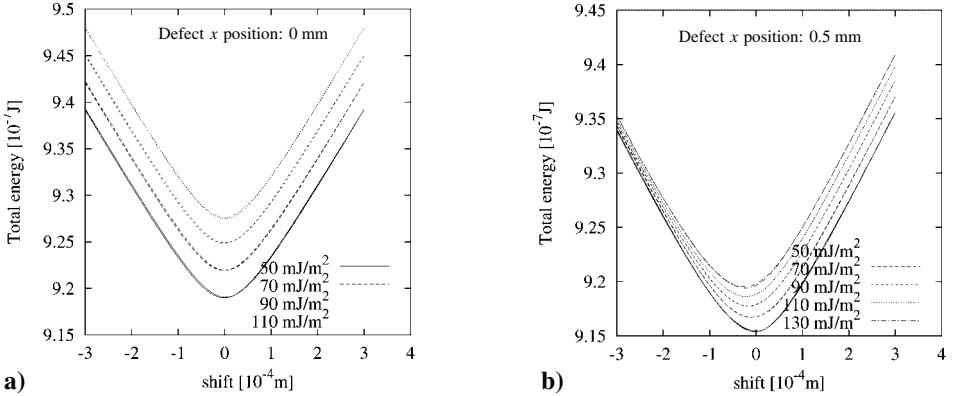


Figure 1.1.23. Total energy for a line defect, placed at the binding site edge, versus a parallel shift displacement. The defect is placed (a) at the binding site center, (b) at the binding site edge.

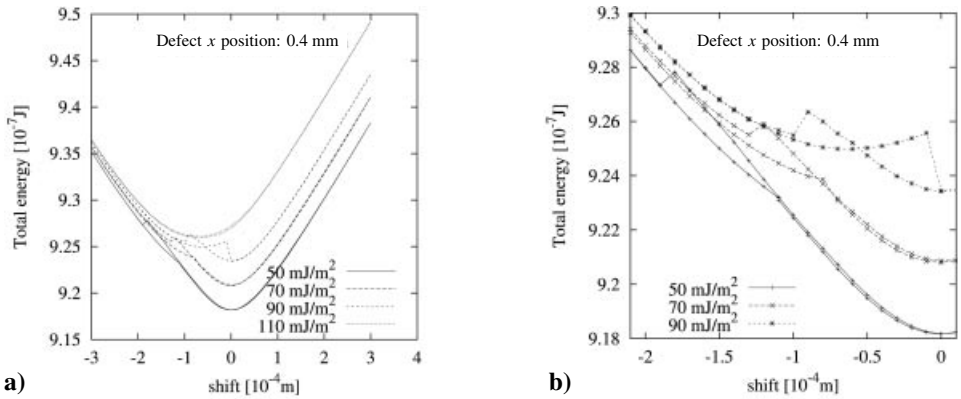


Figure 1.1.24. Total energy for a line defect, placed at $x = 0.4$ mm, versus a parallel shift displacement. Curve (b) zoom on the region where snap-through (hysteresis) occurs.

ergy curve to be combined of both extremes, depending on position: For the micropart right of a certain position, complete wetting is achieved and the curve is similar to Figure 1.1.23 a. When the micropart moves further to the left side, the liquid meniscus shows a sudden snap-through behavior, and the energy curve changes to a curve similar to Figure 1.1.23 b, with the local minimum at an even further misaligned position. The position of this snap-through point depends on the direction of the motion. For the motion from left to right, the point lies further to the right than for the inverse direction, thus a hysteresis is visible in both the energy and the force.

However, the impact of this effect is mitigated by the decrease of the energy curve slope near the misaligned local minimum. This corresponds to a lower

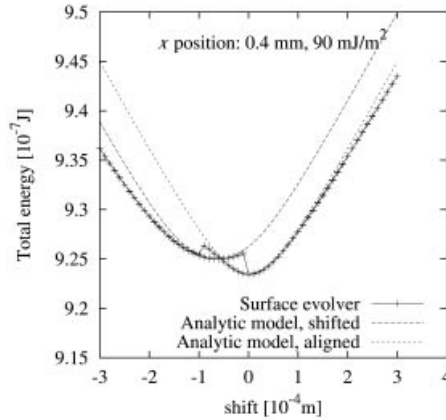


Figure 1.1.25. Comparison between the *Surface Evolver* results and the analytic model. An excellent agreement is found for a large displacement range.

Table 1.1.2. Analytic model parameters for the simulation of a line defect.

Defect position	4×10^{-4} m
Defect amplitude	58 mJ/m ²
Defect width	5×10^{-5} m
Offset energy	8.07×10^{-7} J

force restoring the misaligned position, so that it is easier to leave the local minimum at the misaligned state than the global one at the aligned state. A small force weakening is already visible at Figure 1.1.23 b.

The comparison of the two curves for the analytic model and the *Surface Evolver* results shows an excellent agreement (see Figure 1.1.25). The model parameters are listed in Table 1.1.2.

We performed further simulations to investigate the effect of point defects. Figure 1.1.27 shows the energy curves for a micropart which is rotated about the z axis with a point defect placed at the position $x = 0.2$ mm and $y = 0.35$ mm. Apart from the energy offset, only a very small influence on the energy curve was observed. However, point defect may alter the lateral motion.

We performed a shift simulation with a point defect on one corner (right side) of the path, but this time, the y coordinate of the micropart was adapted according to the ratio of forces in x and y direction. While at the forward pass (right to left) no alteration of the path appeared, the path of the micropart changed as it had passed the equilibrium point (Figure 1.1.26), continuing at a 45° angle from the previous path. This causes a stiffening in the x direction, since the total deflection now is $\sqrt{2}$ times higher than the x component.

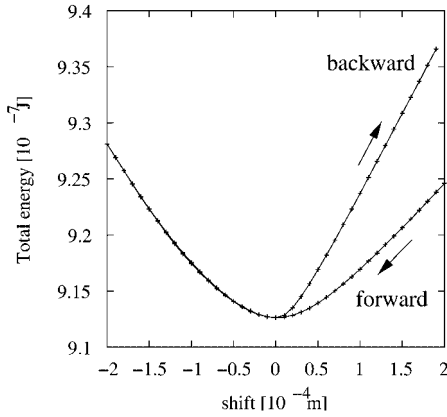


Figure 1.1.26. Stiffening effect of a point defect on the energy curve. The micropart passes the equilibrium and then continues on a different path.

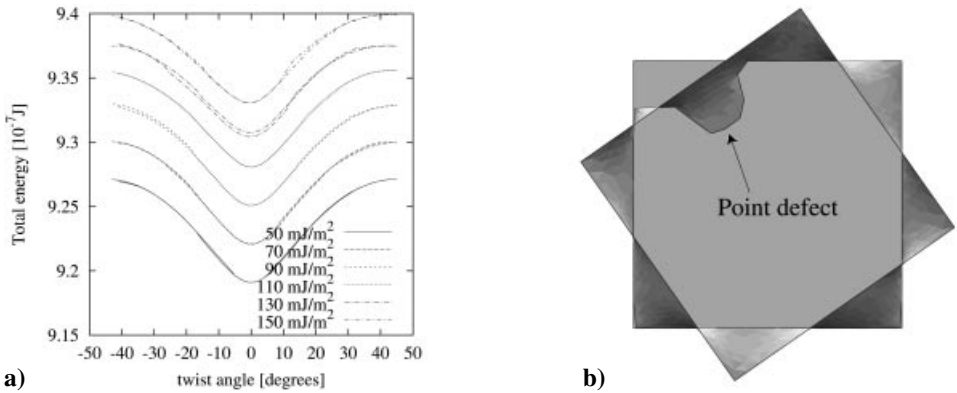


Figure 1.1.27. Total energy for twist sweep with point defect. The micropart faces have been omitted from (b) so as to show the meniscus.

1.1.5.4.2 Inhomogeneous Glue Hardening

Microfluidic self-assembly is a promising technique for producing products with a large amount of equal components like pixel displays. While the exact parallel alignment of simple light emitting diodes is usually rather insignificant, interconnections may impose tighter constraints on the angular position of the micropart. If on the other hand mirrors or directed light sources like LASERS are assembled, deviations of a fraction of degrees can render the device defective.

Assuming a perfect alignment by the capillary forces, it is thus desirable to analyze the sensitivity of the angular position to the hardening process.

The polymerization process is usually initialized by thermally breaking a special lubricant component, the starter molecule, into two radicals. These radicals

function as starting point of the polymer chains by breaking a triethylglycole dimethacrylate monomer into two parts and forming a bond to one of them. Since the resulting molecule is again radicalic, the process continues, until the chain reaction is stopped by the reaction of two radicals.

This process leads to a volume shrinkage; the volume of the polymer is lower than that of the initially available monomer, since the molecules are now arranged much tighter. Experiments show that this volume shrinkage can amount to $\beta = 20\%$.

For the proposed self-assembly process, benzoyl peroxide is used as starter molecule. Benzoyl peroxides are known to break in the presence of non-noble metals in a catalytic reaction at temperatures far below the thermal breakup temperature. Since the self-assembled monolayer is deposited on a gold film which needs several adhesive metal layers above, exposure of the lubricant to other metals is probable at the corner of the micropart. This simulation therefore assumes that due to a defect of the micropart the reaction starts at one corner of the setup and continues spherically through the lubricant until all of it is polymerized. Due to the high aspect ratio of lateral extent and height of the glue, this can be approximated by cylindrical growth.

The micropart has three degrees of freedom, the angle ϕ , lateral motion x , and the height z (see Figure 1.1.28).

The simulation procedure is explained in detail elsewhere [47]. The three major steps are as follows.

1. Find the equilibrium state of the system by minimizing the free energy consisting of interfacial surface energy and the elastic energy of the already hardened glue.
2. Increase the radius of the polymerized glue by constraining the yet liquid glue such that it does not touch the region occupied by the polymerized glue. Decrease the volume of the liquid glue by the volume of the monomer used up by the polymerization.
3. Adjust the calculation of the elastic energy so as to reflect the glue hardened in the current time step.

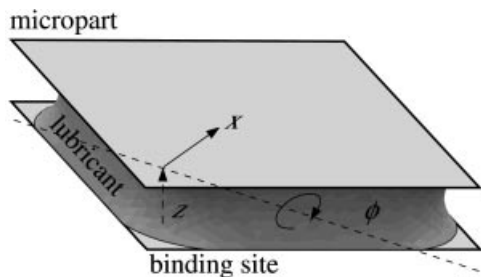


Figure 1.1.28. The degrees of freedom for the simulation of the inhomogeneous glue hardening.

The angular deflection elastic energy is modeled by a spring model $E = K_\phi \phi^2 / 2$ with K_ϕ the spring constant for the degree of freedom ϕ . The remaining degrees of freedom are modeled analogously. Since the shape of the hardened glue is influenced by the degrees of freedom of the micropart, the zero point of the spring model must be adapted for every time step.

From time step t_0 to $t_0 + \Delta t$, the radius of the hardened glue cylinder increases from r_0 to $r_0 + \Delta r$. A new cylindrical layer is formed on the elastic block. The shape of this new part is determined by the current position of the micropart. The equilibrium point of this spring ring therefore depends on the system coordinates at t_0 . A later deflection from this position will lead to an increase in the elastic energy stored in that spring by $\Delta E = \frac{1}{2} k(r(t_0)) \Delta r (\phi - \phi_0(r(t_0)))^2$, where $k(r) = dK_\phi / dr$ and $\phi_0(r)$ is the ϕ deflection when the glue was hardened up to a radius of r .

We then can express the elastic energy for the complete hardened glue with radius r by

$$\begin{aligned} E(r, \phi) &= \frac{1}{2} \int_0^r k(\xi) [\phi - \phi_0(\xi)]^2 d\xi \\ &= \frac{1}{2} \phi^2 \int_0^r k(\xi) d\xi - \phi \int_0^r k(\xi) \phi_0(\xi) d\xi + \frac{1}{2} \int_0^r k(\xi) \phi_0^2(\xi) d\xi \\ &= c_2 \phi^2 + c_1 \phi + c_0 \end{aligned} \quad (28)$$

This reduces to three easy updates for each integration step.

$$c_0(r + \Delta r) \approx c_0(r) + \frac{1}{2} \phi_0^2(r) [K_\phi(r + \Delta r) - K_\phi(r)] \quad (29)$$

$$c_1(r + \Delta r) \approx c_1(r) - \phi_0(r) [K_\phi(r + \Delta r) - K_\phi(r)] \quad (30)$$

$$c_2(r + \Delta r) = \frac{1}{2} K_\phi(r + \Delta r) \quad (31)$$

The spring constant K_ϕ was calculated with the finite elements software package ANSYS [48].

To model the volume shrinkage of the glue, for an increase dV_G of the polymerized volume, the monomer volume V_M is decrease by $dV_M = -dV_G / (1 - \beta)$. For a change in the glue radius from $r_1 = r$ to $r_2 = \Delta$, this evaluates to

$$\Delta V_M = -\frac{1}{1 - \beta} \left[\frac{\pi}{4} (r_2^2 - r_1^2) z_c - \frac{\sqrt{2}}{3} (r_2^3 - r_1^3) \tan \phi \right] \quad (32)$$

with z_c the z position of the chip corner where the polymerization has started.

We performed simulations for different shrink ratios β and Young's moduli Y by scaling the spring constants appropriately. The hardened glue radius increase per simulation step was set to $\Delta r = 10^{-5}$ m.

The results of the simulation are shown in Table 1.1.3 and Figure 1.1.29. For some combinations of β and Y , two values are listed. This is due to a relaxation of the tilt angle ϕ during the simulation run (see Figure 1.1.30). This relaxation is especially distinctive for high volume shrink rates. Since for high β the amount of liquid lubricant becomes small, the interface area to water surrounding the liquid also becomes smaller, until the torque exercised by the elasticity of the hardened glue is greater than the surface tension forces. The first line of the table denotes the maximum angle, while the second line denotes the final angle

Table 1.1.3. Tilting angle (in degrees) of the micropart as a function of Young's modulus Y and shrinking ratio β . Values in parentheses were noisy.

β	Y (MPa)							
	10	20	40	80	150	300	750	2000
0.2	0.0857	0.0657	(0.0372)	(0.0411)	0.0171	0.0114	0.00728	0.00308
0.4	0.266	0.185	0.127	0.0835	0.0576	0.0296	0.0171	0.00568
0.6	0.655	0.462	0.336	0.232	0.157	0.106	0.0648	0.0277
0.7	0.991	0.711	0.504	0.356	0.240	0.168	0.0899	0.0430
		0.710					0.0898	
0.8	1.63	1.20	0.862	0.617	0.435	0.305	0.167	0.0818
	1.62	1.19	0.856	0.614	0.433	0.304	0.166	0.0816
0.9	3.49	2.62	1.95	1.41	1.00	0.678	0.366	0.160
	3.33	2.54	1.90	1.39	0.99	0.670	0.362	0.159
0.95	5.36	4.70	3.49	2.49	1.78	1.20	0.666	0.323
	5.35	4.59	3.30	2.38	1.72	1.17	0.651	0.317

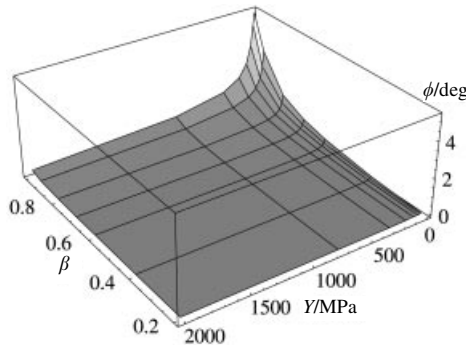


Figure 1.1.29. 3D plot of the results in Table 1.1.3. High tilt angles are expected for high β and low Y .

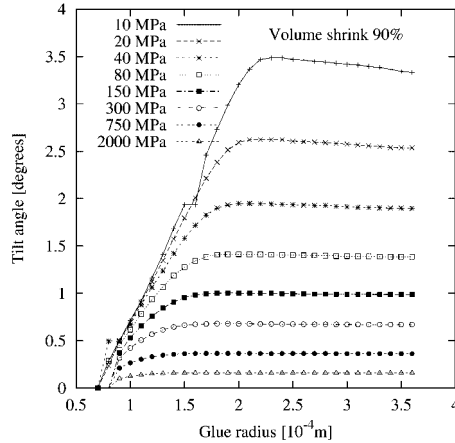


Figure 1.1.30. Micropart tilting angle versus hardened glue radius for a volume shrink ratio of $\beta = 0.9$.

after 30 steps. The final angle is only printed if it differs in the accuracy of the table.

High β values are unlikely to occur in polymerization processes, but are common in drying processes, where most of the lubricant evaporates or dilutes or diffuses into the surrounding liquid medium.

The results clearly show that the final tilt angle both depends on Young's modulus and the volume shrink ratio, and may achieve values of up to 5° . The tilt angle depends also on the lubricant height; again, thinner lubricants work towards smaller errors.

However, the system presented above is not very sensitive to tilt errors due to the low volume shrink ratio $\beta = 20\%$ and the high Young modulus of 2000 MPa.

The results offer a possibility for a new process to obtain defined tilt angles; by carefully choosing a material and introducing a defined starting point for the polymerization, production of defined tilt angles is possible.

1.1.6 Summary and Conclusions

In this chapter we have discussed a surface tension-driven micro-assembly technique with focus on the assembly and self-alignment process. Experimental design and simulation results of the technique are presented. We have performed simulations including calculations of the surface tension-driving force for the assembly, geometry design for the binding site, and investigations of perturbation influence on the assembly results. The experimental results accord with the simulation results. In addition, we have derived several analytical models to predict

the driving forces in fluidic self-assembly, developed geometric calculations of the surface area and the overlap of the binding sites, and outlined preliminary algorithms for optimization of binding site design. By applying the simulation tools to different configurations, we can reduce extensive experimental effort and achieve optimal experimental design.

As an enabling technique, the assembly approach is applicable to generic parts such as surface mount LEDs. We believe that parallel self-assembly is feasible and essential for the production of microsystems. It is anticipated that this self-assembly technique can be applicable to a wide range of micro- or nanoparts made of different materials, for the integration and packaging of complex heterogeneous systems.

1.1.7 Acknowledgments

We would like to thank Roger T. Howe and Uthara Srinivasan for inspiring discussions. We thank Weihua Wang and Daniel T. Schwartz for help in the development of multi-batch assembly techniques. We thank Jiandong Fang, Yanbing Wang and Shenghsiong Liang for help in the fabrication and all the members of the University of Washington MEMS lab and the staff and users of the Washington Technology Center Microfabrication laboratory for their help and support.

This research is supported in part by NSF Career Award ECS9875367 and NSF Award ECS0223598 to K. Böhringer and by donations from Agilent Technologies, Intel Corporation, Microsoft Research, Tanner Research Inc., and Technic Inc. Y. Hanein acknowledges partial support by NSF CISE Postdoctoral Research Associateship EIA0072744. X. Xiong acknowledges support from a Ford Fellowship.

1.1.8 References

- [1] Ralis, S.J., Vikramaditya, B., Nelson, B.J., *IEEE Trans. Electron. Packaging Manuf.* **23** (2000) 123–131.
- [2] Yang, G., Gaines, J.A., Nelson, B.J., in: *Proc. IEEE Int. Conf. Robotics and Automation (ICRA)*, Seoul, South Korea, 2001, pp. 133–138.
- [3] Thompson, J.A., Fearing, R.S., in: *Proc. IEEE/RSJ Int. Conf. Intelligent Robots and Systems (IROS)*, Maui, HI, 2001, pp. 1327–1334.
- [4] Saitou, K., Wang, D.A., Wou, S.J.: *ASME/IEEE J. Microelectromechanical Systems* **9** (2000) 336–346.
- [5] Fearing, R.S., in: *Proc. IEEE/RSJ Int. Conf. Robotics and Intelligent Systems (IROS)*, Pittsburgh, PA, 1995, pp. 212–217.

- [6] Cohn, M.B., Böhringer, K.F., Noworolski, J.M., Singh, A., Keller, C.G., Goldberg, K.Y., Howe, R.T., in: *Proc. SPIE Micromachining and Microfabrication Process Technology IV* (Ed.: Smith, J.H.), Vol. 3511, Santa Clara, CA, International Society for Optical Engineering, September 1998, pp. 2–16.
- [7] Holmes, A.S., Saidam, S.M., *ASME/IEEE J. Microelectromechanical Systems* **7** (1998) 416–422.
- [8] Yeh, H.-J.J., Smith, J.S., in: *IEEE Photon. Technol. Lett.* **6** (1994) 706–708.
- [9] Böhringer, K.F., Goldberg, K.Y., Cohn, M.B., Howe, R.T., Pisano, A.P., in: *IEEE Int. Conf. Robotics and Automation (ICRA)*, Leuven, Belgium, 1998, pp. 483–496.
- [10] Böhringer, K.F., Fearing, R.S., Goldberg, K.Y., in: *The Handbook of Industrial Robotics* (Ed.: Nof, S.), 2nd edn. John Wiley, 1999, pp. 1045–1066.
- [11] Terfort, A., Bowden, N., Whitesides, G.M., *Nature* **386** (1997) 162–164.
- [12] Terfort, A., Whitesides, G.M., *Adv. Mater.* **10** (1998) 470–473.
- [13] Gracias, D., Tien, J., Breen, T.L., Hsu, C., Whitesides, G.M., *Sciences* **289** (2000) 1170–1172.
- [14] Srinivasan, U., Howe, R.T., Liepmann, D., in: *Int. Conf. Solid-State Sensors and Actuators*, Proc. Transducers, Sendai, Japan, 7–10 June 1999, pp. 1170–1173.
- [15] Srinivasan, U., Howe, R.T., Liepmann, D., *J. Microelectromechanical Systems* **10** (2001) 17–24.
- [16] Jacobs, H.O., Tao, A.R., Schwartz, A., Gracias, D.H., Whitesides, G.M., *Science* **296** (2002) 323–325.
- [16a] Yellen, B., Friedman, G., *Magnetic driven assembly of colloidal particles onto patterned surfaces*, in: Technical Proceedings of the 2003 Nanotechnology Conference and Trade Show, Vol. 3 (2003)
- [17] Xiong, X., Hanein, Y., Wang, W., Schwartz, D.T., Böhringer, K.F., in: *Proc. Int. Conf. Solid-State Sensors and Actuators*, Transducers, Munich, Germany, June 2001.
- [18] Xiong, X., Hanein, Y., Fang, J., Wang, Y., Wang, W., Schwartz, D.T., Böhringer, K.F., Technical Report UWEETR-2002-0006, Department of Electrical Engineering, University of Washington, Seattle, USA, March 2002.
- [19] De Gennes, P.G., *Rev. Mod. Phys.* **57** (1985) 827–863.
- [20] Landau, L.D., Lifschitz, E.M., *Course of Theoretical Physics*, Pergamon Press, Vol. 5 and 6, 1969.
- [21] Landau, L.D., Lifschitz, E.M., *Course of Theoretical Physics.*, Pergamon Press, Vol. 6, 1987.
- [22] Popov, Y.O., Witten, T.A., *Eur. Phys. J. E* **6** (2001) 211–220.
- [23] Israelachvili, J., *Intermolecular and Surface Forces*, 2nd edn., Academic Press, 1991.
- [24] Darhuber, A.A., Troian, S.M., Wagner, S., *J. Appl. Phys.* **90** (2001) 3602–3609.
- [25] Darhuber, A.A., Troian, S.M., Davis, J.M., Miller, S.M., Wagner, S., *J. Appl. Phys.* **88** (2000) 5119–5126.
- [26] Lee, J., Kim, C.J., in: *ASME/IEEE J. Microelectromechanical Systems* **9** (2000) 171–180.
- [27] Harsh, K.F., Irwin, R.S., Lee, Y.C., in: *Proc. 1998 Int. Instrum. Symp. (ISA)*, Reno, NV, 1998, pp. 256–261.
- [28] Srinivasan, U., Fluidic Self-Assembly of Microfabricated Parts to Substrates Using Capillary Forces. PhD Thesis University of California at Berkeley, Department of Chemical Engineering, 2001.
- [29] Syms, R.R.A., *J. Microelectromechanical Systems* **4** (1995) 177–184.
- [30] Wale, M.J., Edge, C., in: *IEEE Trans. Components, Hybrids, and Manufacturing Technology* **13** (1990) 780–786.
- [31] Hosokawa, K., Shimoyama, I., Miura, H., *Sensors Actuators A* **57** (1996) 117–125.

- [32] Sato, K., Hata, S., Shimokohbe, A., in: *Proc. SPIE, Int. Symp. Microelectronics and Micro-Electro-Mechanical Systems MICRO/MEMS'99*, Queensland, Australia, 1999, pp. 321–329.
- [33] Sato, K., Ito, K., Hata, S., Shimokohbe, A., in: *Proc. Am. Soc. Precision Engineering*, 15th Annual Meeting, Arizona, USA, Vol. 22, 2000, pp. 345–348.
- [34] Münzing Chemie GmbH, Additives for surface and substrates, January 2001.
- [35] Park, J.Y., Ha, J.S., Kang, C.S., Shin, K.S., Kim, M.I., Jung, J.P., *J. Microelectron. Packaging Soc.* **7** (2000) 63–68.
- [36] Xiong, X., Hanein, Y., Wang, W., Schwartz, D.T., Böhringer, K.F., in: *Proc. Int. Conf. Intelligent Robots and Systems*, Maui, HI, IEEE/RSJ IROS, October–November 2001.
- [37] Bain, C.D., Troughton, E.B., Tao, Y.-T., Evall, J., Whitesides, G.M., Nuzzo, R.G., *J. Am. Chem. Soc.* **111** (1989) 321–335.
- [38] Pojman, J.A., West, W.W., Simmons, J., *J. Chem. Education* **74** (1997) 727–730.
- [39] Lienemann, J., Modeling and simulation of the fluidic controlled self-assembly of micro parts. Diplomarbeit, IMTEK, Albert Ludwig University, Freiburg, Germany, 28 May 2002.
- [40] Brakke, K.A., *Exp. Math.* **1** (1992) 141–165.
- [41] Brakke, K.A., *Surface Evolver Manual*, Mathematics Department, Susquehanna University, Selingsgrove, 18 August 1999.
- [42] Greiner, A., Lienemann, J., Korvink, J.G., Xiong, X., Hanein, Y., Böhringer, K.F., in: *Fifth Int. Conf. Modeling Simulation of Microsystems (MSM'02)*, Tech. Proc. MSM, San Juan, Puerto Rico, USA, 22–25 April 2002.
- [43] Böhringer, K.F., Srinivasan, U., Howe, R.T., in: *IEEE Workshop on Micro Electro Mechanical Systems (MEMS)*, Interlaken, Switzerland, 21–25 January 2001.
- [44] Berger, R., Delamarche, E., Lang, H.P., Gerber, C., Gimzewski, J.K., Meyer, E., Güntherodt, H.-J., *Science* **276** (1997) 2021–2024.
- [45] Noh, J., Hara, M., Molecular-scale growth processes of alkanethiol self-assembled monolayers on Au(111). *Riken Rev.* **38** (2001) 49–51.
- [46] Lienemann, J., Greiner, A., Korvink, J.G., in: *Symp. Design, Test, Integration, and Packaging of MEMS/MOEMS 2002*, Vol. 4755, Cannes-Mandelieu, France, International Society for Optical Engineering, May 2002, pp. 55–63.
- [47] Lienemann, J., Greiner, A., Korvink, J.G., in: *4th Int. Conf. Adv. Semiconductor Devices and Microsystems (ASDAM 2002)*, Smolenice Castle, Slovakia, October 2002, pp. 369–372.
- [48] ANSYS Inc., *ANSYS User's manual Revision 5.7*. Canonsburgh, USA, 2000, <http://www.ansys.com>.

List of Symbols and Abbreviations

Symbol	Designation
a	contact line segment
a	extent of wetted binding site
a_x, a_y	defect shape parameter
A	area
α	angle between displacement and contact line
α_0	electronic polarizability
b	displacement component perpendicular to contact line
b	micropart length
β	apex angle
β	relative volume shrinkage
C	constant
c	pad width
D	defect shape function
d	displacement
δ	variation
Δ	change
E	energy
ϵ_0	permittivity of free space
ϵ_r	relative permittivity
F	force
γ	interfacial/surface tension
I	ionization potential
h	distance between binding site and micropart
K	spring constant
k	Boltzmann constant
L	liquid phase
l	arclength
l	line perpendicular to displacement
l	pad length
l_d	defect size
\mathbf{l}	distance vector
\mathcal{L}	contact line
M	surrounding medium
p	pressure
ϕ	tilt angle
q	charge
R	radius
r, \vec{r}	distance
S	substrate, solid surface
s, s', s''	length of a surface patch (projection, flat, curved)

Symbol	Designation
\vec{s}	triangle edge
T	absolute temperature
t	time
θ	contact angle
θ	micropart orientation
u	projection of curved lubricant side wall onto substrate plane
\mathbf{u}	dipole moment
V	volume
W	work
w	potential energy of interaction
w	projection of contact line
ξ	displacement
Y	Young's modulus
Abbreviation	Explanation
CAE	computer-aided engineering
DI water	deionized water
IPA	isopropyl alcohol
LED	light emitting diode
SAM	self-assembled monolayer
TEGDMA	triethyleneglycol dimethacrylate
UV	ultraviolet
3D	three-dimensional
2D	two-dimensional